



## Extended lattice space of TiO<sub>2</sub> hollow nanocubes for improved sodium storage



Jianze Feng<sup>a</sup>, Yunfa Dong<sup>a</sup>, Yingchun Yan<sup>a</sup>, Weinan Zhao<sup>a</sup>, Tiantian Yang<sup>a</sup>, Jingtang Zheng<sup>b</sup>, Zhongtao Li<sup>a,\*</sup>, Mingbo Wu<sup>a,\*</sup>

<sup>a</sup> State Key Laboratory of Heavy Oil Processing, Institute of New Energy, College of Chemical Engineering, China University of Petroleum (East China), Qingdao 266580, China

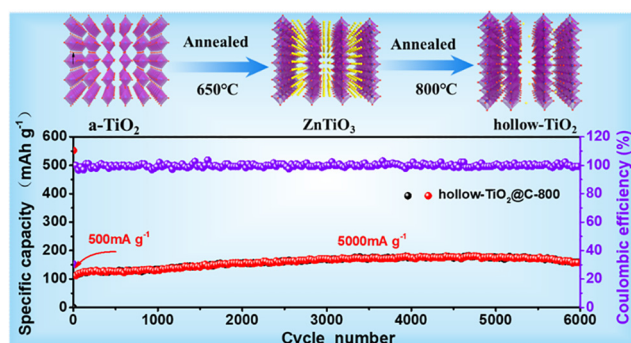
<sup>b</sup> State Key Laboratory of Molecular Engineering of Polymers (Fudan University), China

### HIGHLIGHTS

- The lattice spacing of TiO<sub>2</sub> is enlarged, which facilitates Na<sup>+</sup> desorption/insertion.
- The hollow porous structure could expose numerous surface-redox active sites.
- The N-doped hollow carbon framework could boost the conductivity.

### GRAPHICAL ABSTRACT

A unique hollow TiO<sub>2</sub>/carbon nanocubes (hollow-TiO<sub>2</sub>@C-800) with enlarged lattice spacing of TiO<sub>2</sub> have been synthesized through decomposition of ZnTiO<sub>3</sub> at high temperature, which exhibits a superior cycling stability (154.6 mAh g<sup>-1</sup> after 6000 cycles at 5000 mA g<sup>-1</sup>) and an excellent rate capability (150 mAh g<sup>-1</sup> at 8000 mA g<sup>-1</sup>).



### ARTICLE INFO

#### Keywords:

Nanocubes  
Sodium ion battery  
Anode  
Lattice spacing

### ABSTRACT

Sodium-ion batteries (SIBs) are considered as promising new-fashioned energy storage devices. Among these anode materials of SIBs, the low specific capacity and poor rate capability of TiO<sub>2</sub> are two significant factors of hindering the widely application. Here, a unique hollow TiO<sub>2</sub>/carbon nanocubes (hollow-TiO<sub>2</sub>@C-800) with enlarged lattice spacing of TiO<sub>2</sub> have been synthesized. Experimental results demonstrate that the enlarged lattice spacing of TiO<sub>2</sub> could facilitate Na ions desorption/insertion and inhibit the irreversible side reactions, resulting in fast Na ion transfer kinetics. Moreover, N-doped hollow porous carbon framework could boost the conductivity, inhibit the agglomeration of the smaller TiO<sub>2</sub> and shorten the distance for Na<sup>+</sup> transfer, which lead to lower mechanical stresses and smaller capacity loss during cycles. As expected, hollow-TiO<sub>2</sub>@C-800 shows a superior cycling stability (154.6 mAh g<sup>-1</sup> after 6000 cycles at 5000 mA g<sup>-1</sup>) and an excellent rate capability (150 mAh g<sup>-1</sup> at 8000 mA g<sup>-1</sup>). This simple synthetic method would open a new avenue to prepare the superior SIBs anode.

\* Corresponding authors.

E-mail addresses: [liztao@upc.edu.cn](mailto:liztao@upc.edu.cn) (Z. Li), [wumb@upc.edu.cn](mailto:wumb@upc.edu.cn) (M. Wu).

<https://doi.org/10.1016/j.cej.2019.05.065>

Received 13 February 2019; Received in revised form 9 May 2019; Accepted 11 May 2019

Available online 13 May 2019

1385-8947/ © 2019 Elsevier B.V. All rights reserved.

## 1. Introduction

Lithium-ion batteries have progressively achieved the commercialization mainly used in portable electrical and large energy storage (eg electric vehicles) equipments in recent years [1–3]. Unfortunately, the increasing price of lithium induced by the conflict of the limited lithium resources and the increasing demand for large-scale energy storage (eg grid-scale storage), finding a new energy storage technology to replace the LIBs is becoming an imperative choice [4–6]. Recently, Sodium-ion batteries (SIBs) are sweeping rapidly due to the lower cost and abundant resources of sodium [3,7–9]. Significant efforts have been devoted to develop SIBs anode materials, however, there are still many inherent defects to impede their application. For example, the graphite-based carbon anode is not suitable as SIBs anode due to the limited layer spacing for  $\text{Na}^+$  insertion/deinsertion [10–13]. Some soft and hard carbons exhibit a high reversible capacity over  $200 \text{ mAh g}^{-1}$  at  $1 \text{ A g}^{-1}$ , but the problem of  $\text{Na}^+$  dendrite is caused by the lower voltage plateau versus sodium (below  $0.1 \text{ V}$ ) [14,15]. Although the alloying materials of tin and antimony based complex could store a great number of sodium, but they often face the fast capacity fade due to structural breakage, which is induced by the huge volume change [11,16–18]. Therefore, it still exists a great challenge to develop a suitable anode with ultra-stable cycle life and significant rate performance for SIBs.

As a promising material for SIBs,  $\text{TiO}_2$  has triggered intensively study due to low cost, environment friendly, safer insertion potential and high durability [19–21]. However, the poor electronic conductivity and low capacity of bare  $\text{TiO}_2$  limit their application in sodium storage. To overcome these issues, constructing carbon/ $\text{TiO}_2$  nanohybrid is regarded as an effective way to improve the materials' conductivity and capacity, such as porous carbon coated  $\text{TiO}_2$  or  $\text{TiO}_2$  anchored on porous carbon [19,22,23], both of which exhibit the larger capacity and accelerate charges and ions transferability. For example, He et al. reported the  $\text{TiO}_2/\text{C}$  composite with several morphologies, which can be adjusted to nanoparticles, microrods, rod-in-tube structures, or microtubes by controlling the types of reaction solvents and time. Among these materials, rod-in-tube  $\text{TiO}_2$  with a uniform carbon coating shown the best sodium storage capability (such as a superior rate capability of  $125.2$  at  $10 \text{ A g}^{-1}$ ) [24]. Zhang et al presented a nanocomposite of  $\text{TiO}_2/\text{C}$  nanosheets with highly exposed (001) facets and gorgeous carbon layer coating, this composite displayed an improved sodium storage behavior such as a considerable specific capacity of  $92.9 \text{ mAh g}^{-1}$  after 4000 cycles at  $5 \text{ A g}^{-1}$  due to the synergistic effect between outer carbon layer and inner  $\text{TiO}_2$  nanosheets [25]. Meanwhile, heteroatom doped  $\text{TiO}_2$  technology is also a practical method to improve the electrochemical properties, which could overcome the intrinsic defect of electronic conductivity and facilitate  $\text{Na}^+$  transfer. For instance, flower-like  $\text{TiO}_2$  with S doping nanostructure was reported by He et al, which possessed an extraordinary sodium storage performance (such as a ultra-high capacity of  $254.2$  at  $50 \text{ mA g}^{-1}$ ) [26]. In addition, elaborate controlling the nanostructure of  $\text{TiO}_2$  shows a great potential in increasing the sodium storage capability of Ti-based materials, through which could expose more active sites and improve pseudocapacitive ions storage behavior [27–31]. Therefore, delicately designing and synthesizing hollow  $\text{TiO}_2$  nanohybrids with large surface area would boost sodium storage performance.

Recently, enlarging lattice distance of crystalized anode materials have been reported, which could significantly boost sodium storage capability, because enlarging lattice spacing would facilitate ions diffusion and insertion, inhibit the irreversible side reactions. Meanwhile, enlarging the lattice spacing would decrease the volume change of active material to achieve an ultra-stable capacity [32]. However, none of such kinds of  $\text{TiO}_2$ -based materials have been reported so far. Herein, we first timely propose a template-sacrifice method to convert the amorphous  $\text{TiO}_2$  coated ZIF-8 (a- $\text{TiO}_2@/\text{ZIF-8}$ ) to the hollow cubic Nano complex (hollow- $\text{TiO}_2/\text{C-800}$ ) through pyrolysis. The lattice spacing of

rutile  $\text{TiO}_2$  nanoparticles could be enlarged due to the evaporation of Zn from  $\text{ZnTiO}_3$  precursor at elevated temperature. As a consequence, the enlarging lattice spacing of rutile  $\text{TiO}_2$ , hollow porous structure and conductive carbonic matrix could corporately facilitate Na ions desorption and insertion, inhibit the irreversible side reactions and boost ion transport and sodium storage. Because of the synergistic effects of aforementioned structural merits, this complex shows one of the best cycling stability ( $154.6 \text{ mAh g}^{-1}$  after 6000 cycles at  $5 \text{ A g}^{-1}$ ) and rate capability ( $297 \text{ mAh g}^{-1}$  at  $0.1 \text{ A g}^{-1}$  and  $150 \text{ mAh g}^{-1}$  at  $8 \text{ A g}^{-1}$ ) among  $\text{TiO}_2$  anode.

## 2. Experimental section

### 2.1. Materials synthesis

#### 2.1.1. Synthesis of the ZIF-8 nanotube

$0.6325 \text{ g Zn}(\text{NO}_3)_2 \cdot 6\text{H}_2\text{O}$  was dissolved in  $30 \text{ ml}$  methanol, meanwhile,  $1.5 \text{ g}$  2-methylimidazole and  $9 \text{ mg}$  cetyltrimethylammonium-bromide (CTAB) were dissolved in  $10 \text{ ml}$  methanol. Then, the 2-methylimidazole solution is quickly added to the  $\text{Zn}(\text{NO}_3)_2$  solution. The mixture was stirred at room temperature for  $4 \text{ h}$  and incubated  $10 \text{ h}$ . The resulting precipitate was centrifuged and washed three times with ethanol before drying at  $60^\circ\text{C}$ .

#### 2.1.2. Synthesis of the a- $\text{TiO}_2@/\text{ZIF-8}$

$0.2 \text{ g}$  ZIF-8 was homogeneously dissolved in  $100 \text{ ml}$  ethanol by ultrasonication. Followed by added  $0.3 \text{ g}$  hexadecylamine (HAD) and  $0.7 \text{ ml}$   $\text{NH}_3 \cdot \text{H}_2\text{O}$  to the above solution with stirring for  $10 \text{ min}$ . Then,  $1.2 \text{ ml}$  titanium isopropoxide (TIP, 97%) was added to the dispersion and stirred for another  $60 \text{ min}$ . The white product was dried at  $80^\circ\text{C}$  after collected by centrifuged and washed with ethanol for several times. The obtained amorphous  $\text{TiO}_2$  coating ZIF-8 denoted as a- $\text{TiO}_2@/\text{ZIF-8}$ .

#### 2.1.3. Synthesis of the $\text{TiO}_2/\text{C-500}$

The a- $\text{TiO}_2@/\text{ZIF-8}$  was annealed in nitrogen at  $500^\circ\text{C}$  for  $2 \text{ h}$  with a heating rate of  $2^\circ\text{C min}^{-1}$ , the final product features amorphous property and denoted as  $\text{TiO}_2/\text{C-500}$ .

#### 2.1.4. Synthesis of the $\text{TiO}_2/\text{C-650}$

The a- $\text{TiO}_2@/\text{ZIF-8}$  was annealed in nitrogen at  $650^\circ\text{C}$  for  $2 \text{ h}$  with a heating rate of  $2^\circ\text{C min}^{-1}$  to obtain the mixture of rutile  $\text{TiO}_2$ ,  $\text{ZnTiO}_3$  and C. The product denoted as  $\text{TiO}_2/\text{C-650}$ .

#### 2.1.5. Synthesis of the hollow- $\text{TiO}_2/\text{C-800}$

To synthesis the final product of hollow- $\text{TiO}_2/\text{C-800}$ . The  $\text{TiO}_2@/\text{ZIF-8}$  was annealed in nitrogen at  $800^\circ\text{C}$  for  $2 \text{ h}$  with a heating rate of  $2^\circ\text{C min}^{-1}$ .

#### 2.1.6. Synthesis of the $\text{TiO}_2$

The preparation of the  $\text{TiO}_2$  is similar to the preparation of the h- $\text{TiO}_2/\text{C-800}$  expect to not addition of  $0.2 \text{ g}$  ZIF-8 to the  $100 \text{ ml}$  ethanol under stirring for  $60 \text{ min}$ .

### 2.2. Materials characterization

X-ray powder diffraction (XRD) is employed an X-ray diffractometer with Cu K $\alpha$  radiation from  $10$  to  $60^\circ$  to analyze the crystalline structure and phase composition. The microstructures of the as-obtained samples were analyzed by using field emission scanning electron microscopy (SEM, Hitachi S-4800). Transmission electron microscopy (TEM) were carried out on JEM-2010 system at  $220 \text{ kV}$ . X-ray photoelectron spectroscopy (XPS, Thermo Scientific Escalab 250XI) with Mg K $\alpha$  radiation was carried out to determine the microscopic material composition (elemental composition and chemical bonding).  $\text{N}_2$  adsorption-desorption isotherms of samples were determined and analyzed by the

Brunauer-Emmette-Teller (BET) method (Autosorb-iQ, Quantachrome). Fourier transform infrared spectra (FTIR) were detected on a PerkinElmer spectrum GX FTIR system. Thermogravimetric analysis (TGA) was determined under air flow from room temperature to 800 °C with a heating rate of 10 °C min<sup>-1</sup> (using STA 409 PC Luxx, Netzsch-Gerätebau).

### 2.3. Electrochemical measurements

The electrochemical performance tests were carried out through using CR2032-type coin cells with pure Na foil as the counter electrode assembled in an argon-filled glove box (H<sub>2</sub>O < 0.1 ppm, O<sub>2</sub> < 0.1 ppm). To the working electrodes, the as-prepared materials (80 wt%), Super P (10 wt%) and poly(vinylidene fluoride) (PVDF) (10 wt% in N-methyl-2-pyrrolidinone (NMP) solvent) were mixing to form a homogeneous slurry. The mixture was then pasted on Cu foil and dried in a vacuum oven at 80 °C for 12 h, the material loading was about 1.0–1.4 mg cm<sup>-2</sup> on each round copper foil (The capacity was calculated based on the mass of whole composite.), the sodium ion electrolyte consists of 1 M NaClO<sub>4</sub> in ethylene carbonate/diethyl carbonate (1/1; v/v) with 5 wt% fluoroethylene carbonate. The galvanostatic charge/discharge measurement was performed by a multichannel battery testing system (LAND CT2001A) with a voltage range of 0.01–3 V. Both cyclic voltammetry (CV) at a scan rate of 0.1–100 mV s<sup>-1</sup> and electrochemical impedance spectroscopy (EIS) at a frequency range of 100 kHz to 10 mHz with AC amplitude of 5 mV were carried on CHI760D electrochemical workstation. All of the measurements were performed at room temperature.

## 3. Results and discussion

The preparation process of the hollow-TiO<sub>2</sub>@C-800 nanocomposite is depicted in Fig. 1: the nanocubes of ZIF-8 were adopted as template and then coated by amorphous TiO<sub>2</sub> (namely a-TiO<sub>2</sub>@ZIF-8) through hydrolysis of tetra-n-butyl titanate (TIP). During subsequent pyrolysis of a-TiO<sub>2</sub>@ZIF-8, the Zn in ZIF-8 core section was gradually diffused into the lattice of coated TiO<sub>2</sub> to form ZnTiO<sub>3</sub> and then evaporated at higher temperature. Due to the high melting point and stiff structure of TiO<sub>2</sub>, the lattice spacing is increased after escaping of Zn. Finally, the hollow TiO<sub>2</sub> nanocubes (hollow-TiO<sub>2</sub>@C-800) are formed with the advanced features for sodium storage, such as conductive matrix, porous hollow structure and enlarged lattice spacing.

The X-ray diffraction (XRD) profiles of the a-TiO<sub>2</sub>@ZIF-8, TiO<sub>2</sub>@C-500, TiO<sub>2</sub>@C-650 and hollow-TiO<sub>2</sub>@C-800 are shown in Fig. 2a. The

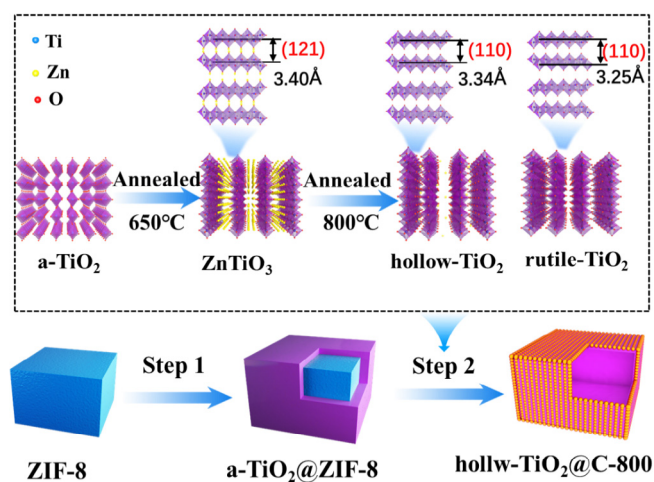
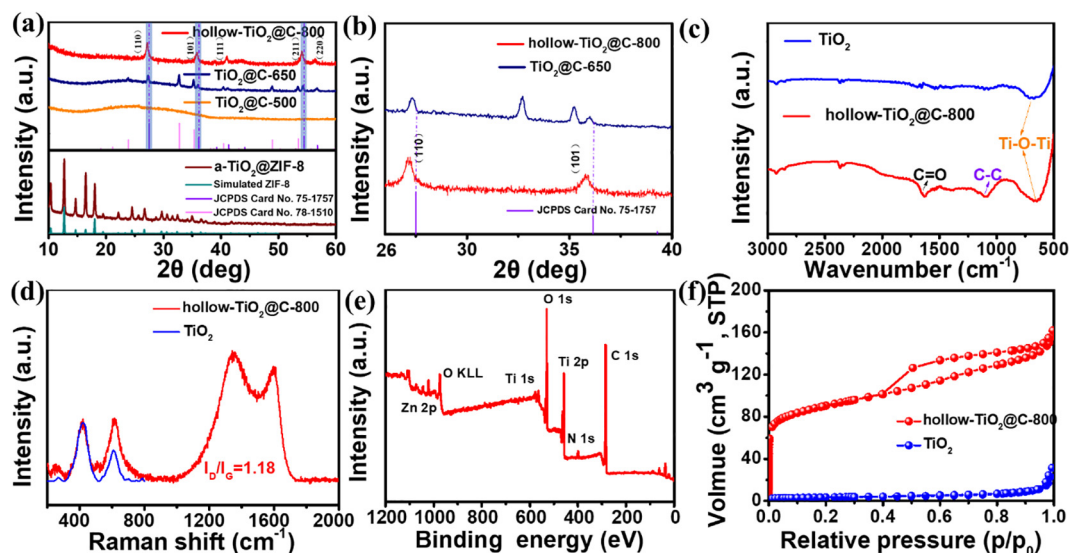


Fig. 1. Schematic illustration of the preparation of hollow-TiO<sub>2</sub>@C-800 hollow nanocube. Step 1. deposition of TiO<sub>2</sub> onto ZIF-8. Step 2. Annealing reaction under N<sub>2</sub>.

profile of a-TiO<sub>2</sub>@ZIF-8 shows the same diffraction peaks as ZIF-8, which indicates the amorphous structure of TiO<sub>2</sub> coating. When a-TiO<sub>2</sub>@ZIF-8 annealed at 500 °C, no diffraction peaks can be observed in TiO<sub>2</sub>@C-500 due to the gradually decomposition of ZIF-8 crystals during elevating temperature. As shown in Fig. 2a and Fig. 2b, once the annealing temperature rise up to 650 °C, the diffraction peaks of TiO<sub>2</sub>@C-650 could be divided into crystallized rutile TiO<sub>2</sub> and ZnTiO<sub>3</sub>, which would ascribe to the crystallized TiO<sub>2</sub> and recrystallization of diffused Zn from ZIF-8 core with part of TiO<sub>2</sub> on shell. After pyrolysis at 800 °C, all of the diffraction peaks of ZnTiO<sub>3</sub> in TiO<sub>2</sub>@C-650 were converted to rutile TiO<sub>2</sub> in hollow-TiO<sub>2</sub>@C-800, except slightly left shifts than that in JCPDS Card No. 75-1757 [33]. The lattice spacing of (1 1 0) planes was enlarged from 0.328 nm (rutile TiO<sub>2</sub>) to 0.334 nm (hollow-TiO<sub>2</sub>@C-800) and the lattice constant was also increased from (rutile TiO<sub>2</sub>: a = 4.5937, b = 4.5937, c = 2.9587) to (hollow-TiO<sub>2</sub>@C-800: a = 4.6001, b = 4.6001, c = 2.9603) (Table S1), which would be attributed to the Zn doped into TiO<sub>2</sub> and followed by the evaporation of Zn at higher temperature.

As shown in Fourier transform infrared spectra (FTIR), the profiles of both hollow-TiO<sub>2</sub>@C-800 and TiO<sub>2</sub> exhibit same peaks at 650 cm<sup>-1</sup>, which is attributed to Ti-O-Ti vibration of TiO<sub>2</sub> (Fig. 2c) [32]. Besides, the additional peaks at 1200 cm<sup>-1</sup> and 1600 cm<sup>-1</sup> of hollow-TiO<sub>2</sub>@C-800 are assigned to the vibration of C-C and C = O bonds from the carbonated ZIF-8 [11]. Thermogravimetric analysis (TGA) is performed from room temperature to 800 °C to determine the components of hollow-TiO<sub>2</sub>@C-800 composite. In Fig. S1, the 3% weight loss from 25 °C to 200 °C is attributed to the evaporation of adsorbed gas and free water [34]. The weight loss of 13% between 360 °C and 580 °C is assigned to the combustion of carbonic subunits [33]. The Raman spectra of hollow-TiO<sub>2</sub>@C-800 and TiO<sub>2</sub> are shown in Fig. 2d, both of which exhibit two scattering bands of TiO<sub>2</sub> at 413 and 618 cm<sup>-1</sup>, which demonstrates that Zinc as dopant diffused into the lattice of TiO<sub>2</sub> after the decomposition of ZnTiO<sub>3</sub> instead of aggregation. Additionally, the D band located at 1,350 cm<sup>-1</sup> and G band near 1,588 cm<sup>-1</sup> are related to the disordered and ordered structure of carbon material, respectively [35–37]. The I<sub>D</sub>/I<sub>G</sub> of hollow-TiO<sub>2</sub>@C-800 is calculated as 1.18, indicating more disordered carbon to accelerate the electronic/ion transfer. X-ray photoelectron spectroscopy (XPS) is employed to characterize the element composition and chemical state of the as-synthesized hollow-TiO<sub>2</sub>@C-800. As shown in Fig. 2e, the overall spectrum demonstrates the existence of Ti, Zn, C, O and N (high-resolution images of C 1s, Ti 2p, O 1s and Zn 2p are shown in Fig. S2) [34,38]. Fig. S3 is the high-resolution spectrum of N1s that have been deconvoluted into two peaks, which are ascribed to the pyridinic N (398.12 eV) and pyrrolic N (400.14 eV). Doping N atom into carbon architecture could introduce more active sites and facilitate the charge transfer, which could significantly enhance the Na storage capability [39]. Meanwhile, the Table S2 shows that there is only 0.7 at% of Zn in this composite, the tiny amount of Zn indicates that most Zn have been evaporated at high temperature. In addition, The high-resolution Zn 2p spectrum (Fig. S2d) shows that the Zn is bivalent in the composite which serves as a structural support to enlarge spaces between the lattice interlayers [40,41]. Fig. 2f and Fig. S4 are the BET surface areas and pore-size distribution of the hollow-TiO<sub>2</sub>@C-800 and TiO<sub>2</sub>. TiO<sub>2</sub> exhibits a small specific surface area of 12 m<sup>2</sup> g<sup>-1</sup>. However, the specific surface area of hollow-TiO<sub>2</sub>@C-800 increased to 168 m<sup>2</sup> g<sup>-1</sup> with hierarchical porosity, which is mediating the diffusion of Na<sup>+</sup> [42,43].

The scanning electron microscopy (SEM) and transmission electron microscope (TEM) are used to verify the nanostructures. The as-prepared ZIF-8 are consisted with uniform nanocubes with an average size of 200 nm (Fig. 3a and Fig. S5). After TiO<sub>2</sub> coating, the morphology of most nanocubes are reserved in a-TiO<sub>2</sub>@ZIF-8 (Fig. 3b). After pyrolysis, hollow-TiO<sub>2</sub>@C-800 are also consisted of well-defined nanocubes (Fig. 3c). The transmission electron microscope (TEM) images is employed to detect the inside structure of these materials (Fig. 3d, e and Fig. S6). When TiO<sub>2</sub>@ZIF-8 was annealed in N<sub>2</sub> at 500 °C (Fig. S6a), the



**Fig. 2.** (a) XRD patterns of a-TiO<sub>2</sub>@ZIF-8, TiO<sub>2</sub>@C-500, TiO<sub>2</sub>@C-650 and hollow-TiO<sub>2</sub>@C-800. (b) XRD patterns of TiO<sub>2</sub>@C-650 and hollow-TiO<sub>2</sub>@C-800. (c) FT-IR spectra of hollow-TiO<sub>2</sub>@C-800 and TiO<sub>2</sub>. (d) Raman spectra of hollow-TiO<sub>2</sub>@C-800 and TiO<sub>2</sub>. (e) XPS survey spectrum of hollow-TiO<sub>2</sub>@C-800. (f) N<sub>2</sub> adsorption/desorption isotherm of hollow-TiO<sub>2</sub>@C-800 and TiO<sub>2</sub> architecture.

obtained TiO<sub>2</sub>@C-500 still exhibit the similar nanocubes structure as precursor. After annealed at 650 °C, a coating layer is appeared on the surface of nanocubes in TiO<sub>2</sub>@C-650 (Fig. 3d and S6b), which would be attributed to the formation of ZnTiO<sub>3</sub>. Increasing the temperature to 800 °C, the well-defined hollow nanocubes are formed in hollow-TiO<sub>2</sub>@C-800 during the decomposition of ZIF-8 and ZnTiO<sub>3</sub>, which are composed of many loosely ultrafine TiO<sub>2</sub> nanoparticles anchored on the carbon framework (Fig. 3e). The elemental mapping images of hollow-TiO<sub>2</sub>@C-800 (Fig. 3f) also confirm the homogenous distribution of Ti, C, Zn, N and O. The high-resolution transmission electron microscope (HRTEM) images show the *d*<sub>110</sub> lattice fringe of TiO<sub>2</sub> particles in hollow-TiO<sub>2</sub>@C-800 is 0.334 nm (inset in Fig. 3e), which is larger than

that in bare TiO<sub>2</sub> (0.325 nm in Fig. S6d). The corresponding Selected Area Electron Diffraction (SAED) pattern of hollow-TiO<sub>2</sub>@C-800 (inset in Fig. 3e) are also well coincidence to the diffraction peaks of XRD pattern (in Fig. 2a).

The sodium storage behaviors of hollow-TiO<sub>2</sub>@C-800 and TiO<sub>2</sub> are evaluated in half-cell SIBs with a voltage window of 0.01–3 V. The CV curve of hollow-TiO<sub>2</sub>@C-800 is shown in Fig. 4a. Two peaks are appeared at 1.3 V and 0.57 V at first cycle and disappeared in the following scans, which ascribed to the formation of the solid electrolyte interface (SEI) film and irreversible Na<sup>+</sup> insertion [44,45]. After the initial cycle, only one broad anodic peak that located at 0.82 V is detected, which is ascribed to the desodiating reaction of anode material

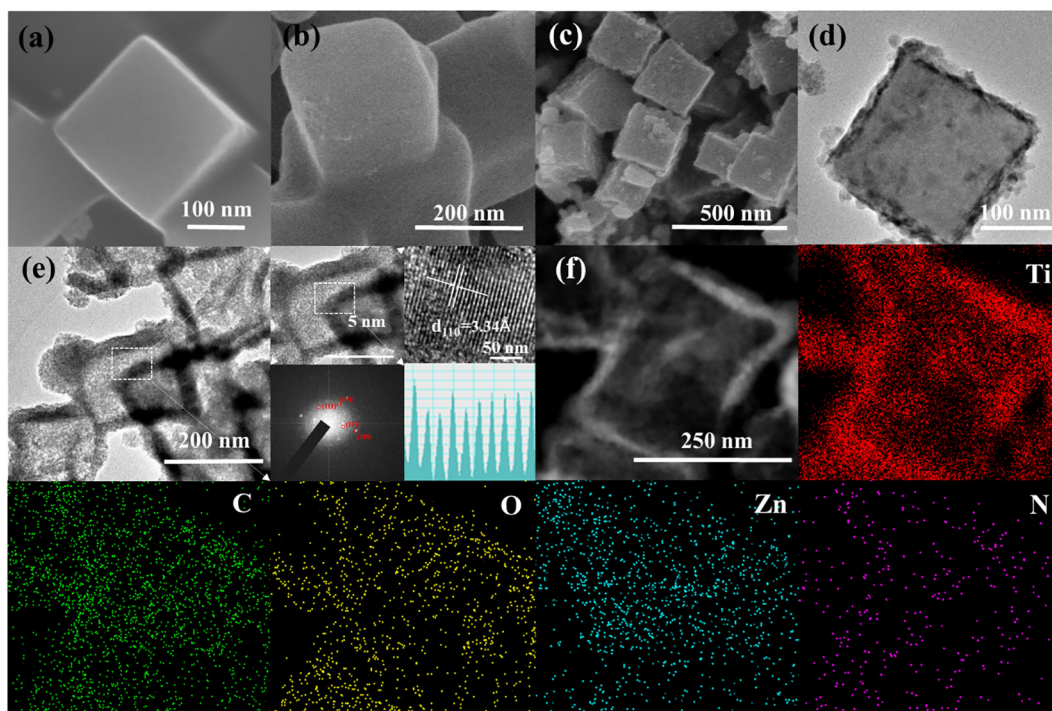


**Fig. 3.** SEM images: (a) ZIF-8, (b) a-TiO<sub>2</sub>@ZIF-8, (c) hollow-TiO<sub>2</sub>@C-800. TEM image of (d) TiO<sub>2</sub>@C-650. (e) hollow-TiO<sub>2</sub>@C-800. Right: HRTEM and SAED patterns of hollow-TiO<sub>2</sub>@C-800. (f) Element mapping images of hollow-TiO<sub>2</sub>@C-800.

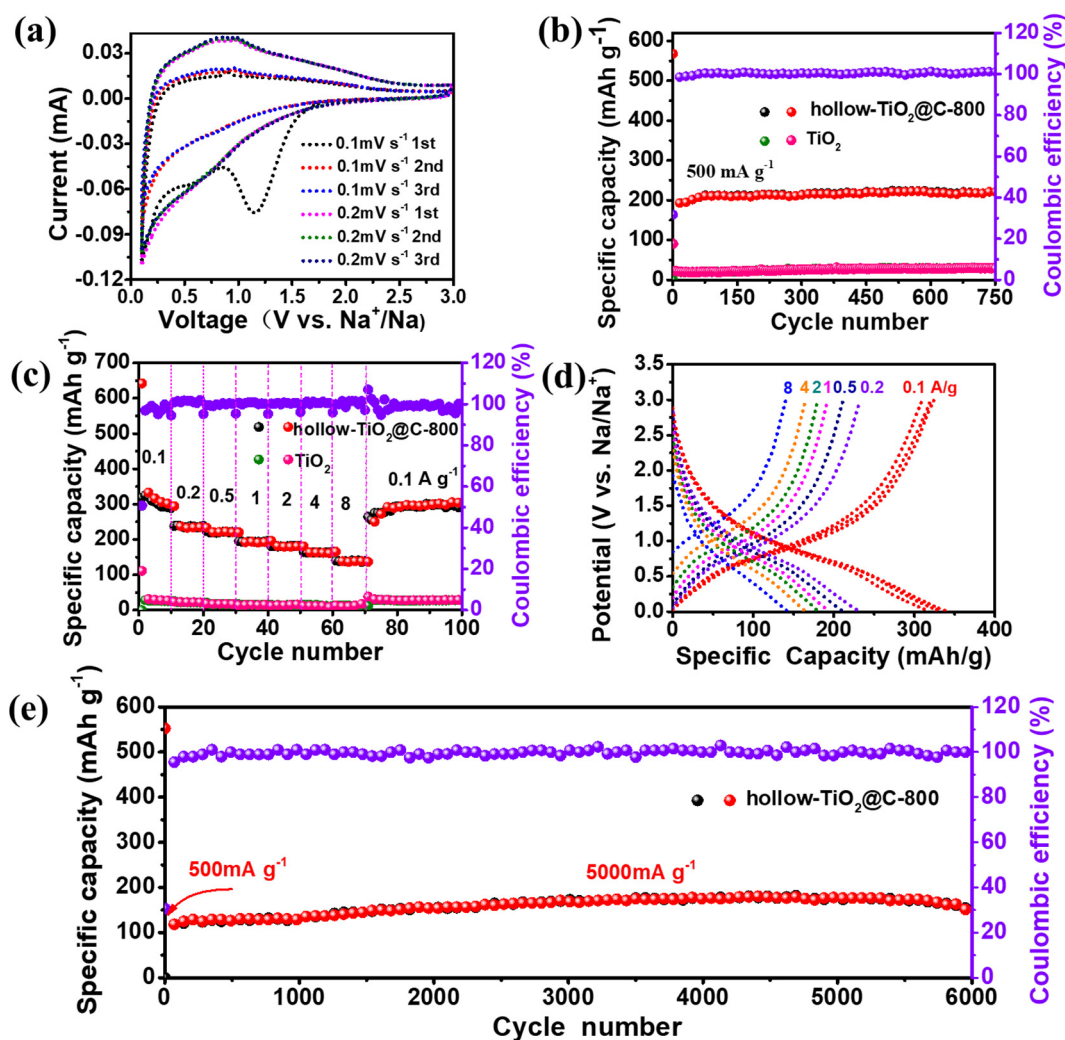


**Fig. 4.** Electrochemical characterization of hollow-TiO<sub>2</sub>@C-800 and TiO<sub>2</sub> for sodium ion storage. (a) Cyclic voltammograms of hollow-TiO<sub>2</sub>@C-800 (scan rate: 0.1 mV s<sup>-1</sup> and 0.2 mV s<sup>-1</sup>). (b) Capacity retentions and Coulombic efficiency of hollow-TiO<sub>2</sub>@C-800 and TiO<sub>2</sub> at 500 mA g<sup>-1</sup>. (c) Rate performance of hollow-TiO<sub>2</sub>@C-800 and TiO<sub>2</sub>. (d) Charge/discharge profiles of hollow-TiO<sub>2</sub>@C-800 at different rates. (e) Capacity retentions and Coulombic efficiency of hollow-TiO<sub>2</sub>@C-800 at 5000 mA g<sup>-1</sup> (precycling at current of 500 mA g<sup>-1</sup> for 5 cycles).

with Na<sup>+</sup> (the redox reaction of Ti<sup>3+</sup>/Ti<sup>4+</sup>) [19,23]. Specially, there is no obvious cathodic peak, which would be due to that the hollow porous structure of hollow-TiO<sub>2</sub>@C-800 has a great number of facile-to-access surface-redox active sites to boost ion transport and charge transfer [46]. The cycling performance of hollow-TiO<sub>2</sub>@C-800 and TiO<sub>2</sub> are evaluated at 500 mA g<sup>-1</sup> in Fig. 4b. TiO<sub>2</sub> only maintains a capacity of 40 mAh g<sup>-1</sup> after 750 cycles. While, hollow-TiO<sub>2</sub>@C-800 shows a reversible capacity at 205 mAh g<sup>-1</sup>. The higher capacity of hollow-TiO<sub>2</sub>@C-800 is attributed to the hollow structure and the enlarged lattice spacing. Fig. 4e displays the long cycling performance of hollow-TiO<sub>2</sub>@C-800 at 5000 mA g<sup>-1</sup> with the 99% coulombic efficiency, which could be delivered a reversible capacity at 154.6 mAh g<sup>-1</sup> after 6000 cycles, suggesting an ultrastable cycling performance than state-of-the-art (Table S3). From the TEM image of hollow-TiO<sub>2</sub>@C-800 in Fig. S7 after 6000 cycles at 5000 mA g<sup>-1</sup>, some nanocubes still persevered, demonstrating the robustness of the nanostructure.

The rate capability of hollow-TiO<sub>2</sub>@C-800 and TiO<sub>2</sub> are shown in Fig. 4c. With the increasing of current density, reversible capacities of 297, 230, 202, 190, 175, 165 and 150 mAh g<sup>-1</sup> are achieved at 100, 200, 500, 1000, 2000, 4000 and 8000 mA g<sup>-1</sup>, respectively. When the current density return back to 100 mA g<sup>-1</sup>, the capacity of hollow-TiO<sub>2</sub>@C-800 still maintain at 298 mAh g<sup>-1</sup>. The galvanostatic charge/discharge curves for hollow-TiO<sub>2</sub>@C-800 at various current densities

are displayed in Fig. 4d, the plateaus located at 0.81 V are preserved with the increasing of current density, which indicates the superior stability at higher rate. However, the TiO<sub>2</sub> electrode exhibits ultra-low capacity under the same condition.

Electrochemical impedance spectroscopy (EIS) is employed to assess the kinetic of hollow-TiO<sub>2</sub>@C-800 and TiO<sub>2</sub> in Fig. S8. h-TiO<sub>2</sub>@C-800 displays a lower charge transfer resistance, which could boost the electrode kinetics and lead to an improved rate performance [11,47,48]. The excellent rate performance of hollow-TiO<sub>2</sub>@C-800 would be due to the synergistic effect of hollow structure and enlarged lattice spacing, which could shorten the distance for Na<sup>+</sup> transfer and boost the electrochemical reaction rates. So far, the rate performance of hollow-TiO<sub>2</sub>@C-800 is one of the best TiO<sub>2</sub>-based anodes *in-state-of-art*, such as the SIBs anodes of S-TiO<sub>2</sub> nanocube arrays, protonated titanate nanowire arrays, Single-Crystal-like TiO<sub>2</sub> Graphene, P-TiO<sub>2</sub> nanoarrays, and carbon coated anatase TiO<sub>2</sub> spheres in Fig. S9.

To investigate the electrochemical kinetics, the CV curves of hollow-TiO<sub>2</sub>@C-800 at different scan rate from 0.1 to 100 mV s<sup>-1</sup> are shown in Fig. 5a and Fig. S10. The contribution of capacitance is evaluated by Eq. (1) based on the relationship between peak current (i) and scan rate (v) [49]:

$$i = av^b \quad (1)$$

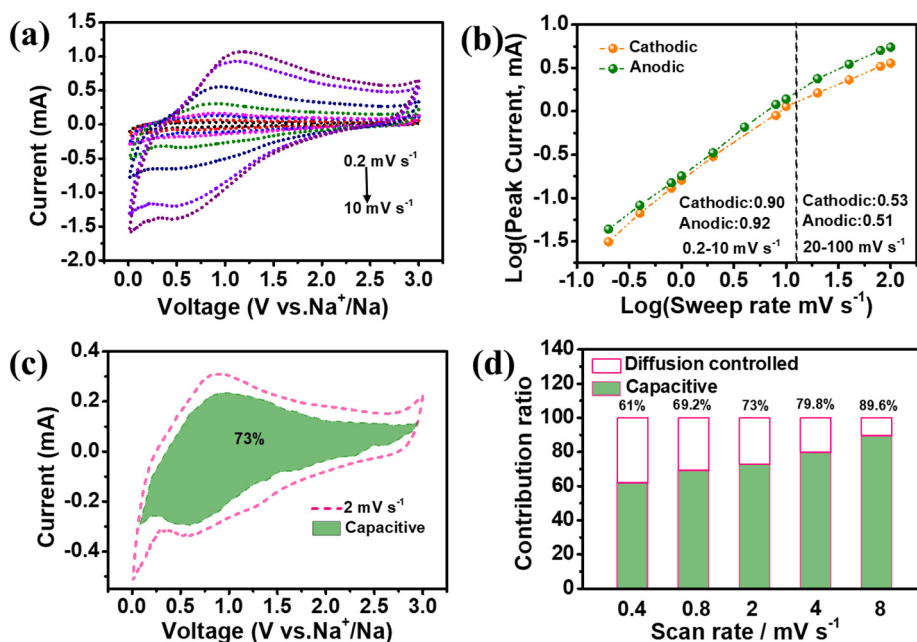


**Fig. 5.** Kinetics analysis of hollow-TiO<sub>2</sub>@C-800. (a) CV curves of hollow-TiO<sub>2</sub>@C-800 at various sweep rates from 0.2 to 10 mV s<sup>-1</sup>. (b) Log (i) versus log (v) profile of hollow-TiO<sub>2</sub>@C-800. (c) the diffusion and capacitive (shaded region) contribution in hollow-TiO<sub>2</sub>@C-800 electrode at a sweep rate of 2 mV s<sup>-1</sup>. (d) Contribution ratio of the capacitive and diffusion-controlled charges at different sweep rates.

where  $b$  is an adjustable index to access the contribution of surface-controlled and diffusion-controlled. The  $b$ -value is 1.0 (0.5) represents the contribution of total surface-controlled (diffusion-controlled), the pseudocapacitor becomes stronger if the  $b$  value is bigger. The  $b$ -values of hollow-TiO<sub>2</sub>@C-800 are 0.90 (or 0.92) in the sweep rate range from 0.2 mV s<sup>-2</sup> to 10 mV s<sup>-2</sup> and 0.53 (or 0.51) in the sweep rate range from 10 mV s<sup>-2</sup> to 100 mV s<sup>-2</sup> for cathodic (or anodic) peak (Fig. 5b), suggesting the dramatically pseudocapacitive behavior of hollow-TiO<sub>2</sub>@C-800. To further identify the capacity contribution of the capacitive charge and diffusion-controlled charge, the CV curves current ( $i$ ) at a certain voltage ( $V$ ) could be decomposed into two parts in following law [11,50]:

$$i = k_1 v + k_2 v^{1/2} \quad (2)$$

$k_1 v$  and  $k_2 v^{1/2}$  represent the surface capacitive-controlled and diffusion-controlled contribution, as shown in Fig. 5c and Fig. 5d, the proportion of capacitive contribution is 73% at 2.0 mV s<sup>-1</sup>. The increasing of capacitive contribution at higher scan rates indicates that the capacitive charge becomes dominant on Na<sup>+</sup> storage in hollow-TiO<sub>2</sub>@C-800 at high current density.

All in all, the improved sodium storage capability of the unique hollow TiO<sub>2</sub> nanohybrids could ascribe to the following synthetic effects: 1. the enlarged lattice spacing could facilitate Na ions desertion and insertion, inhibit the irreversible side reaction, which lead to great rate performance and durability. 2. the hollow porosity structure of hollow-TiO<sub>2</sub>@C-800 could expose numerous facile-to-access surface-redox active sites to boost ion transport and sodium storage. 3. the N-doped hollow carbon framework could increase the conductivity, inhibit the agglomeration of TiO<sub>2</sub> and shorten the distance for Na<sup>+</sup> transfer.

#### 4. Conclusion

A well-defined nanocubes with an amorphous TiO<sub>2</sub> coated ZIF-8 cores have been designed and synthesized, which gradually convert to the hollow nanocubes (hollow-TiO<sub>2</sub>@C-800) at elevated temperature. The shell of the hollow-TiO<sub>2</sub>@C-800 is composed of N-doped carbon matrix “bounded” TiO<sub>2</sub> nanocrystals. While, the lattice spacing of as-prepared TiO<sub>2</sub> nanocrystals is increased during the conversion from ZnTiO<sub>3</sub> to TiO<sub>2</sub> with the increasing of temperature. As the result, the hollow-TiO<sub>2</sub>@C-800 delivers a high reversible capacity (154.6 mAh

g<sup>-1</sup> after 6000 cycles at 5.0 A g<sup>-1</sup>) and ultrahigh rate capability (150 mAh g<sup>-1</sup> at 8.0 A g<sup>-1</sup>) during reversible storage sodium due to the synthetic effects of its advanced features.

#### Acknowledgements

This work was supported by the National Natural Science Foundation of China (Grant Nos. 21572269, 21502227 and 51873231), the Fundamental Research Funds for the Central Universities (17CX05015, 15CX08005A), the Financial Support from Taishan Scholar Project, the Key Research and Development Program of Shandong Province, China (2017GGX40118).

#### Appendix A. Supplementary data

Supplementary data to this article can be found online at <https://doi.org/10.1016/j.cej.2019.05.065>.

#### REFERENCES

- [1] M.M. Thackeray, C. Wolverton, E.D. Isaacs, Electrical energy storage for transportation—approaching the limits of, and going beyond, lithium-ion batteries, *Energy Environ. Sci.* 5 (2012) 7854–7863.
- [2] E. Castel, E. Berg, M. El Kazzi, P. Novák, C. Villavieille, Differential Electrochemical Mass Spectrometry Study of the Interface of xLi<sub>2</sub>MnO<sub>3</sub>(1-x)LiMO<sub>2</sub> (M = Ni, Co, and Mn) Material as a Positive Electrode in Li-Ion Batteries, *Chem. Mater.* 26 (2014) 5051–5057.
- [3] P. Nayak, L. Yang, W. Brehm, P. Adelhelm, From Lithium-Ion to Sodium-Ion Batteries: Advantages, Challenges, and Surprises, *Angew. Chem. Int. Ed.* 57 (2017) 102–120.
- [4] S.-W. Kim, D.-H. Seo, X. Ma, G. Ceder, K. Kang, Electrode Materials for Rechargeable Sodium-Ion Batteries: Potential Alternatives to Current Lithium-Ion Batteries, *Adv. Energy Mater.* 2 (2012) 710–721.
- [5] B. Chen, Y. Meng, J. Sha, C. Zhong, W. Hu, N. Zhao, Preparation of MoS<sub>2</sub>/TiO<sub>2</sub> based nanocomposites for photocatalysis and rechargeable batteries: progress, challenges, and perspective, *Nanoscale* 10 (2017) 34–68.
- [6] D. Larcher, J.M. Tarascon, Towards greener and more sustainable batteries for electrical energy storage, *Nat Chem* 7 (2015) 19–29.
- [7] L. Chen, M. Fiore, J.E. Wang, R. Ruffo, D.-K. Kim, G. Longoni, Readiness Level of Sodium-Ion Battery Technology: A Materials Review, *Adv. Sustainable Syst.* 2 (2018) 1700153.
- [8] M. Lao, Y. Zhang, W. Luo, Q. Yan, W. Sun, S.X. Dou, Alloy-Based Anode Materials toward Advanced Sodium-Ion Batteries, *Adv Mater* 29 (2017) 1700622.
- [9] J. Mei, T. Liao, L. Kou, Z. Sun, Two-Dimensional Metal Oxide Nanomaterials for Next-Generation Rechargeable Batteries, *Adv Mater* 29 (2017) 1700176.
- [10] M. Hu, H. Zhou, X. Gan, L. Yang, Z.-H. Huang, D.-W. Wang, F. Kang, R. Lv, Ultrahigh rate sodium ion storage with nitrogen-doped expanded graphite oxide in

- ether-based electrolyte, *J. Mater. Chem. A* 4 (2018) 7394–7402.
- [11] Z. Li, J. Feng, H. Hu, Y. Dong, H. Ren, W. Wu, Z. Hu, M. Wu, An amorphous tin-based nanohybrid for ultra-stable sodium storage, *J. Mater. Chem. A* 6 (2018) 18920–18927.
- [12] X. Zhao, W. Cai, Y. Yang, X. Song, Z. Neale, H.-E. Wang, J. Sui, G. Cao, MoSe<sub>2</sub> nanosheets perpendicularly grown on graphene with Mo–C bonding for sodium-ion capacitors, *Nano Energy* 47 (2018) 224–234.
- [13] T. Huang, D. Lu, L. Ma, X. Xi, R. Liu, D. Wu, A hit-and-run strategy towards perylene diimide/reduced graphene oxide as high performance sodium ion battery cathode, *Chem. Eng. J.* 349 (2018) 66–71.
- [14] Z.L. Yu, S. Xin, Y. You, L. Yu, Y. Lin, D.W. Xu, C. Qiao, Z.H. Huang, N. Yang, S.H. Yu, J.B. Goodenough, Ion-Catalyzed Synthesis of Microporous Hard Carbon Embedded with Expanded Nanographite for Enhanced Lithium/Sodium Storage, *J. Am. Chem. Soc.* 138 (2016) 14915–14922.
- [15] H. Zhang, W. Zhang, H. Ming, J. Pang, H. Zhang, G. Cao, Y. Yang, Design advanced carbon materials from lignin-based interpenetrating polymer networks for high performance sodium-ion batteries, *Chem. Eng. J.* 341 (2018) 280–288.
- [16] Y. Xu, M. Zhou, C. Zhang, C. Wang, L. Liang, Y. Fang, M. Wu, L. Cheng, Y. Lei, Oxygen vacancies: effective strategy to boost sodium storage of amorphous electrode materials, *Nano Energy* 38 (2017) 304–312.
- [17] H. Gao, J. Niu, C. Zhang, Z. Peng, Z. Zhang, A Dealloying Synthetic Strategy for Nanoporous Bismuth-Antimony Anodes for Sodium Ion Batteries, *ACS Nano* 12 (2018) 3568–3577.
- [18] H. Gao, W. Ma, W. Yang, J. Wang, J. Niu, F. Luo, Z. Peng, Z. Zhang, Sodium storage mechanisms of bismuth in sodium ion batteries: An operando X-ray diffraction study, *J. Power Sources* 379 (2018) 1–9.
- [19] Z. Le, F. Liu, P. Nie, X. Li, X. Liu, Z. Bian, G. Chen, H.B. Wu, Y. Lu, Pseudocapacitive Sodium Storage in Mesoporous Single-Crystal-like TiO<sub>2</sub>-Graphene Nanocomposite Enables High-Performance Sodium-Ion Capacitors, *ACS Nano* 11 (2017) 2952–2960.
- [20] G. Longoni, R.L. Pena Cabrera, S. Polizzi, M. D'Arienzo, C.M. Mari, Y. Cui, R. Ruffo, Shape-Controlled TiO<sub>2</sub> Nanocrystals for Na-Ion Battery Electrodes: The Role of Different Exposed Crystal Facets on the Electrochemical Properties, *Nano Lett* 17 (2017) 992–1000.
- [21] C. Zhao, Y. Cai, K. Yin, H. Li, D. Shen, N. Qin, Z. Lu, C. Liu, H.-E. Wang, Carbon-bonded, oxygen-deficient TiO<sub>2</sub> nanotubes with hybridized phases for superior Na-ion storage, *Chem. Eng. J.* 350 (2018) 201–208.
- [22] K. wang, H. Sohn, S. Yoon, Mesoporous niobium-doped titanium oxide-carbon (Nb-TiO<sub>2</sub>-C) composite as an anode for high-performance lithium-ion batteries, *J. Power Sources* 378 (2018) 225–234.
- [23] B. Li, B. Xi, Z. Feng, Y. Lin, J. Liu, J. Feng, Y. Qian, S. Xiong, Hierarchical Porous Nanosheets Constructed by Graphene-Coated, Interconnected TiO<sub>2</sub> Nanoparticles for Ultrafast Sodium Storage, *Adv Mater* 30 (2018) 1705788.
- [24] H. He, Q. Gan, H. Wang, G.-L. Xu, X. Zhang, D. Huang, F. Fu, Y. Tang, K. Amine, M. Shao, Structure-dependent performance of TiO<sub>2</sub>/C as anode material for Na-ion batteries, *Nano Energy* 44 (2018) 217–227.
- [25] Q. Zhang, H. He, X. Huang, J. Yan, Y. Tang, H. Wang, TiO<sub>2</sub>@C nanosheets with highly exposed (001) facets as a high-capacity anode for Na-ion batteries, *Chem. Eng. J.* 332 (2018) 57–65.
- [26] H. He, D. Huang, W. Pang, D. Sun, Q. Wang, Y. Tang, X. Ji, Z. Guo, H. Wang, Plasma-Induced Amorphous Shell and Deep Cation-Site S Doping Endow TiO<sub>2</sub> with Extraordinary Sodium Storage Performance, *Adv Mater* 30 (2018) 1801013.
- [27] S. Deng, Y. Zhong, Y. Zeng, Y. Wang, X. Wang, X. Lu, X. Xia, J. Tu, Hollow TiO<sub>2</sub>@Co<sub>9</sub>S<sub>8</sub> Core-Branch Arrays as Bifunctional Electrocatalysts for Efficient Oxygen/Hydrogen Production, *Adv. Sci.* 5 (2017) 1700772.
- [28] L. Zhao, Q. Cao, A. Wang, J. Duan, W. Zhou, Y. Sang, H. Liu, Iron oxide embedded titania nanowires—An active and stable electrocatalyst for oxygen evolution in acidic media, *Nano Energy* 45 (2018) 118–126.
- [29] D. Wang, Q. Liu, C. Chen, M. Li, X. Meng, X. Bie, Y. Wei, Y. Huang, F. Du, C. Wang, G. Chen, NASICON-Structured NaTi<sub>2</sub>(PO<sub>4</sub>)<sub>3</sub>@C Nanocomposite as the Low Operation-Voltage Anode Material for High-Performance Sodium-Ion Batteries, *ACS Appl. Mater. Interfaces* 8 (2016) 2238–2246.
- [30] Z. Wei, D. Wang, M. Li, Y. Gao, C. Wang, G. Chen, F. Du, Fabrication of Hierarchical Potassium Titanium Phosphate Spheroids: A Host Material for Sodium-Ion and Potassium-Ion Storage, *Adv. Energy Mater.* 8 (2018) 1801102.
- [31] Z. Zhang, M. Li, Y. Gao, Z. Wei, M. Zhang, C. Wang, Y. Zeng, B. Zou, G. Chen, F. Du, Fast Potassium Storage in Hierarchical Ca<sub>0.5</sub>Ti<sub>2</sub>(PO<sub>4</sub>)<sub>3</sub>@C Microspheres Enabling High-Performance Potassium-Ion Capacitors, *Adv. Funct. Mater.* 28 (2018) 1802684.
- [32] L. Que, F. Yu, L. Zheng, Z. Wang, D. Gu, Tuning Lattice Spacing in Titanate Nanowire Arrays for Enhanced Sodium Storage and Long-Term Stability, *Nano Energy* 45 (2018) 337–347.
- [33] Y. Wang, R. Zhang, Y. Pang, X. Chen, J. Lang, J. Xu, C. Xiao, H. Li, K. Xi, S. Ding, Carbon@titanium nitride dual shell nanospheres as multi-functional hosts for lithium sulfur batteries, *Energy Storage Mater.* 16 (2019) 228–235.
- [34] Z. Yin, J. Qin, W. Wang, M. Cao, Rationally designed hollow precursor-derived Zn<sub>3</sub>V<sub>2</sub>O<sub>8</sub> nanocages as a high-performance anode material for lithium-ion batteries, *Nano Energy* 31 (2017) 367–376.
- [35] X. Zhao, J. Sui, F. Li, H. Fang, H. Wang, J. Li, W. Cai, G. Cao, Lamellar MoSe<sub>2</sub> nanosheets embedded with MoO<sub>2</sub> nanoparticles: novel hybrid nanostructures promoted excellent performances for lithium ion batteries, *Nanoscale* 8 (2016) 17902–17910.
- [36] X. Zhao, H.E. Wang, J. Cao, W. Cai, J. Sui, Amorphous/crystalline hybrid MoO<sub>2</sub> nanosheets for high-energy lithium-ion capacitors, *Chem. Commun.* 53 (2017) 10723–10726.
- [37] X. Zhao, H.-E. Wang, R.C. Massé, J. Cao, J. Sui, J. Li, W. Cai, G. Cao, Design of coherent anode materials with 0D Ni<sub>3</sub>S<sub>2</sub> nanoparticles self-assembled on 3D interconnected carbon networks for fast and reversible sodium storage, *J. Mater. Chem. A* 5 (2017) 7394–7402.
- [38] H. Zhang, Y. Jiang, Z. Qi, X. Zhong, Y. Yu, Sulfur doped ultra-thin anatase TiO<sub>2</sub> nanosheets/graphene nanocomposite for high-performance pseudocapacitive sodium storage, *Energy Storage Mater.* 12 (2018) 37–43.
- [39] S. Huang, Z. Li, B. Wang, J. Zhang, Z. Peng, R. Qi, J. Wang, Y. Zhao, N-Doping and Defective Nanographitic Domain Coupled Hard Carbon Nanoshells for High Performance Lithium/Sodium Storage, *Adv. Funct. Mater.* 28 (2018) 1706294.
- [40] Xu. Danhua, Donghua Fan, Wenzhong Shen, Catalyst-free direct vapor-phase growth of Zn<sub>1-x</sub>Cu<sub>x</sub>O micro-cross structures and their optical properties, *Nanoscale Res. Lett* 8 (2013) 46.
- [41] W. Yang, J. Xiao, Y. Ma, S. Cui, P. Zhang, P. Zhai, L. Meng, X. Wang, Y. Wei, Z. Du, B. Li, Z. Sun, S. Yang, Q. Zhang, Y. Gong, Tin Intercalated Ultrathin MoO<sub>3</sub> Nanoribbons for Advanced Lithium-Sulfur Batteries, *Adv. Energy Mater.* 9 (2019) 1803137.
- [42] B. Chen, N. Zhao, L. Guo, F. He, C. Shi, C. He, J. Li, E. Liu, Facile synthesis of 3D few-layered MoS<sub>2</sub> coated TiO<sub>2</sub> nanosheet core-shell nanostructures for stable and high-performance lithium-ion batteries, *Nanoscale* 7 (2015) 12895–12905.
- [43] M. Yu, J. Li, L. Wang, KOH-activated carbon aerogels derived from sodium carboxymethyl cellulose for high-performance supercapacitors and dye adsorption, *Chem. Eng. J.* 310 (2017) 300–306.
- [44] Y. Liu, M. Guo, Z. Liu, Q. Wei, M. Wei, Rapid and facile synthesis of hierarchically mesoporous TiO<sub>2</sub>-B with enhanced reversible capacity and rate capability, *J. Mater. Chem. A* 6 (2018) 1196–1200.
- [45] H. Xu, Y. Liu, T. Qiang, L. Qin, J. Chen, P. Zhang, Y. Zhang, W. Zhang, W. Tian, Z. Sun, Boosting sodium storage properties of titanium dioxide by a multiscale design based on MOF-derived strategy, *Energy Storage Mater.* 17 (2018) 126–135.
- [46] R. Wang, S. Wang, Y. Zhang, D. Jin, X. Tao, L. Zhang, Graphene-coupled Ti<sub>3</sub>C<sub>2</sub> MXenes-derived TiO<sub>2</sub> mesostructure: promising sodium-ion capacitor anode with fast ion storage and long-term cycling, *J. Mater. Chem. A* 6 (2018) 1017–1027.
- [47] X. Zhao, H.-E. Wang, Y. Yang, Z.G. Neale, R. Massé, J. Cao, W. Cai, J. Sui, G. Cao, Reversible and fast Na-ion storage in MoO<sub>2</sub>/MoSe<sub>2</sub> heterostructures for high energy-high power Na-ion capacitors, *Energy Storage Mater.* 12 (2018) 241–251.
- [48] Y. Wang, Y. Wang, J. Liu, L. Pan, W. Tian, M. Wu, J. Qiu, Preparation of carbon nanosheets from petroleum asphalt via recyclable molten-salt method for superior lithium and sodium storage, *Carbon* 122 (2017) 344–351.
- [49] P. Xiao, F. Bu, R. Zhao, M. Aly Aboud, I. Shakir, Y. Xu, Sub-5 nm Ultrasmall Metal-Organic Framework Nanocrystals for Highly Efficient Electrochemical Energy Storage, *ACS Nano* 12 (2018) 3947–3953.
- [50] Y. Huang, Z. Wang, Y. Jiang, S. Li, M. Wang, Y. Ye, F. Wu, M. Xie, L. Li, R. Chen, Conductivity and Pseudocapacitance Optimization of Bimetallic Antimony-Indium Sulfide Anodes for Sodium-Ion Batteries with Favorable Kinetics, *Adv. Sci.* 5 (2018) 1800613.